Engineering structure and functionalities of chemical vapor deposited photocatalytic titanium dioxide films through different types of precursors

Diane Samélor, Asiya Turgambaeva, Vladislav Krisyuk, Adeline Miquelot, Jérémy Cure, Sergey Sysoev, Sergey Trubin, Pavel Stabnikov, Jérôme Esvan, Vassilios Constandoudis, et al.

Engineering structure and functionalities of chemical vapor deposited photocatalytic titanium dioxide films through different types of precursors

Diane Samélor[1], Asiya Turgambaeva[2], Vladislav Krisyuk[2], Adeline Miquelot[1], Jeremy Cure[3], Sergey Sysoev[2], Sergey Trubin[2], Pavel Stabnikov[2], Jérôme Esvan[1], Vassilios Constandoudis[4], Constantin Vahlas[1,*]

[1] *CIRIMAT-CNRS, 4 allée Emile Monso, BP-44362, 31030 Toulouse Cedex 4, France*

[2] *Nikolaev Institute of Inorganic Chemistry SB RAS, Novosibirsk 630090, Russia*

[3] *LAAS-CNRS, Avenue du Colonel Roche, 31031 Toulouse, France*

[4] *Nanometrisis, TEPA Lefkippos, Patriarchou Grigoriou & Neapoleos 27, PO Box 60037, Agia Paraskevi 15341, Greece*

[*] *Corresponding author. orcid.org/0000-0001-5911-0296 ;*

Email : constantin.vahlas@ensiacet.fr

Abstract

The photocatalytic properties of titanium dioxide TiO_2 thin films, a seminal semiconductor material in solar radiation involving key enabling technologies depend on their structural characteristics which, in turn are monitored by the type and the conditions of the applied deposition technique. In this work, we investigate the physicochemical characteristics of two solid precursors, oxo-β-diketonate $TiO(thd)_2$ (**1**) and mixed alkoxide-β-diketonate $Ti(thd)_2(OBu)_2$ (**2**), for the chemical vapor deposition (CVD) of TiO_2 films as alternatives to the established liquid titanium(IV) isopropoxide (TTIP). We show that vaporization of **1** results in a complex mixture of intermediate species, while that of **2** occurs congruently. Direct liquid injection CVD

from **1**, **2**, and TTIP at 500 °C results in anatase containing, rutile rich two phase films for the first two, and to pure anatase for the latter. Films deposited from **1** and **2** are composed of large grains with limited porosity, with smaller and more densely packed aggregates for the former, which also presents a higher O/Ti ratio in the O-Ti lattice. These differences account for a higher generation rate of H_2 of films from **1**, in the photocatalytic decomposition of water. This comparative experimental information can be useful to build new models for extended and more reliable predictions in a materials by design approach.

1. Introduction

The photocatalytic properties of titanium dioxide TiO_2, a seminal semiconductor material in solar radiation involving key enabling technologies, depend on the presence and ratio of its allotropic forms, and of its structural characteristics such as surface morphology and crystallographic diversification and orientation [1, 2]. These characteristics are driven by the nature of the processing technique and by the operating conditions that are applied for the production of TiO_2. A typical example is the metalorganic chemical vapor deposition MOCVD, which allows the production of a wealth of micro- and nano-structures of TiO_2 films [3-7]. Attempts to correlate the structural and morphological characteristics of MOCVD TiO_2 films with their photocatalytic performance have been reported for the cases of hydrogen production by solar water splitting [3, 8], pollution reduction [9] and antimicrobial applications [10]. In most of these works, the screening of the functional property was performed by varying processing conditions, mainly the deposition temperature [3, 5, 11, 12]. In contrast, the chemistry of the deposition process is less questionable, a large majority of the works on the MOCVD of TiO_2 films being performed from the commercially available titanium(IV) isopropoxide (TTIP or TIPP) compound. However, the question as to whether the source chemistry influences the structural characteristics of TiO_2 films

was already raised in the late nineties through a comparative study of TiO_2 films processed from TTIP and anhydrous titanium(IV) nitrate $Ti(NO_3)_4$ [13]. In that work, screening of composition and morphology as a function of deposition temperature did not result in significant differences of the composition of the films. A qualitative comparison of the films morphologies concluded that in the flux-limited regime, the respective microstructures are indistinguishable, while in the reaction rate-limited regime the differences in microstructures were attributed to different surface events and timescales. Both chemistries resulted in the formation of anatase or rutile for the same range of deposition temperature. There were no results on the photocatalytic properties of the TiO_2 films, processed from the two precursors. Since then, numerous works on the production and characterization of TiO_2 films, indirectly dealt with this question by reporting on various features obtained from different processing environments and conditions. Recently, the question on the effect that a different deposition precursor may have on the characteristics and performance of the films was again investigated, through the introduction of acetyl acetone in a TTIP-based aerosol assited CVD process [14]. In a closer to our perspective, Mathur and coworkers investigated the influence of precursor chemistry on the differential cell growth and biocompatibility on TiO_2 films and found that the nano-morphological features of the films stimulate the cell adhesion and growth [15].

Despite the considerable cost, time and effort dedicated during the past decades to the investigation of TiO_2-based films, strong correlations in the chain processing - structure - optical, electric and electronic properties – photocatalytic performance, still remain rare. This is due to the complex interdependence of carrier photogeneration, carrier concentration, carrier transport, and properties of the surfaces exposed to the aqueous catalytic solutions. Consequently, it is difficult to mine this extended, helter-skelter database in order to feed computational efforts and verify their outcome, with the aim to optimize the claimed need for materials discovery [16].

The present work subscribes to an effort of structuring the experimental information on MOCVD TiO_2 films by providing a common framework for the investigation of various precursors and their influence on the structural and functional characteristics of the obtained films. We perform an in depth comparison of the microstructural features such as the porosity or the specific surface area, and the nature of the deposited allotropic phases of TiO_2 films processed in the same conditions from two precursors, oxo-β-diketonate $TiO(thd)_2$ (**1**) and mixed alkoxide-β-diketonate $Ti(thd)_2(OBu)_2$ (**2**), thd=2,2,6,6-tetramethylheptane-3,5-dionate. We complete the investigation by also investigating in the same conditions TiO_2 films deposited from TTIP as a reference. Figure 1 presents the structural formulas of the three molecular compounds.

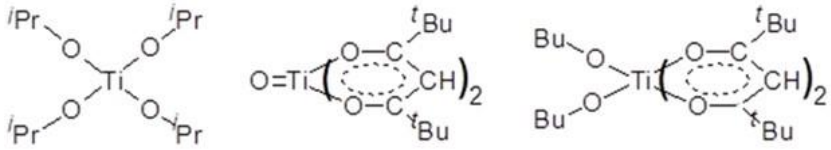

Figure 1. Molecular compounds of Ti, investigated as CVD precursors for TiO_2 films. Titanium tetraisopropoxide (TTIP) left, oxo-β-diketonate $TiO(thd)_2$ (**1**, middle), alkoxide-β-diketonate $Ti(thd)_2(OBu)_2$ (**2**, right). $^{i}Pr = CH(CH_3)_2$, $^{t}Bu = C(CH_3)_3$, $Bu = (CH_2)_3CH_3$.

We extend this comparative investigation uphill to include the thermal properties of **1** and **2** by thermal analysis, tensimetry and mass spectrometry (MS). This part of the work yields information on the composition of the gas phase during evaporation, and during the thermolysis of the precursors' vapors, in a similar way than the one used for the MS investigation of the decomposition of TTIP [17]. We approach the functional properties of the films through a comparative investigation of dihydrogen production from photo-reduction of water. Finally, we discuss the observed correlations prior providing concluding remarks.

2. Experimental section

$[TiO(thd)_2]_2$ (**1**) was prepared by an original technique described earlier [18] starting from $TiCl_4$ and H(thd) in one pot under vigorous bubbling of ammonia. $Ti(OBu)_2(thd)_2$ (**2**) was prepared by a conventional technique in one step starting from $Ti(C_4H_9O)_4$ and H(thd). Both precursors are solid in ambient conditions and readily soluble in organic solvents. **1** is more stable than **2** when manipulated in air. The compounds were purified by vacuum sublimation at 1.3 Pa, and 220 °C and 120 °C for (1) and (2), respectively. TTIP (99.999 %, Sigma-Aldrich) was used without purification.

Thermogravimetric analysis (TGA) of the precursors was performed by a TG 209 F1 Iris (NETZSCH) thermobalance, using a standard Al open crucible. The measurements were taken at atmospheric pressure under 35±5 mL/min He flow, with a 10 °C/min heating ramp. The temperature dependency of the saturated vapor pressure of the precursors was obtained by the flow and Knudsen methods. The flow method is detailed in [19] and consists in passing He flow through a mass of the compound maintained at a predetermined temperature. The vaporized substance is trapped downstream in a cold zone and its mass is measured by weight gain. The saturated vapor pressure is determined with a ±5 % precision. Measurements by Knudsen effusion method with mass spectrometric registration of the gas phase composition were performed using a custom-made setup [20].

The thermal behavior of the precursors during their evaporation and thermolysis was investigated by mass spectrometry. Time-of-flight mass spectrometry was performed with a MSKh-6 instrument, equipped with an evaporator connected with a specially designed system imitating a low pressure hot wall CVD reactor, described in details in [21]. The CVD reactor communicates with the ionization chamber of the mass spectrometer through a 0.2 mm effusion

orifice. Approximately 1 to 2 mg of the compound was placed in an open glass ampoule and kept in the evaporator at a constant temperature of 235 °C for **1** and 110 °C for **2**, under dynamic vacuum conditions. The vaporized compound enters the reactor, whose temperature was varied with a 5 deg/min ramp and the resulting gas phase enters the mass spectrometer and is ionized with 70 eV electrons ionization energy. If needed, a reactant gas, in the present case oxygen, is introduced into the reactor. In the adopted operating conditions, interactions among the molecules in gas phase are excluded, eventual decomposition of the tested molecular compound occurring only on the CVD reactor walls. The gas phase composition was monitored uninterruptedly. Experimental data were obtained as full-range mass spectra recorded every 2 min; they were collected and processed using National Instruments hardware and software. In this way, it was possible to illustrate the evolution of the intensity of selected ion peaks as a function of the temperature of the CVD reactor [22]. Due to the low volatility of **1**, as it will be shown hereafter, direct probe insertion mass spectrometric analysis was additionally performed on a Finnigan MAT 8200 double focusing sector mass spectrometer, operating at 70 eV ionization energy. In this case, the solid precursor was positioned directly into ion source and rapid point heating allowed minimizing the thermal conversions of the sample.

Deposition experiments were performed in a home-made, horizontal hot-wall CVD reactor equipped with various gas lines and mass flow controllers, a direct liquid injection (DLI) system, and a quartz tube (25mm diameter, 300mm length) heated by a resistive furnace [23]. The reactor is schematically presented in Figure S1, in the supporting information (SI) section. A dry pump and pressure gauges connected to the output of the quartz tube were used to keep the total reaction pressure at 1333 Pa. Deposition from all three precursors was performed at 500 °C. Indeed, it will be shown hereafter that, at 500 °C compounds **1** and **2** are fully decomposed, while previous works on the CVD of TiO_2 from TTIP showed that, in these conditions the films are

composed of pure anatase, they are heteroatoms free and they present a nanostructured tree-like columnar morphology [3]. Preliminary experiments revealed different deposition rates in these conditions, depending on the precursor used. Since our aim was to compare the morphology, structure and properties of the films, we targeted similar thicknesses for all and for this reason the deposition time was fixed on purpose at 45 min, 60 min and 50 min for deposition from TTIP, **1** and **2**, respectively. It will be shown hereafter that these conditions yield approximately 300 nm thick films.

12x13x0.38 mm^3 Si samples cut from 4" Si (001) wafers (Sil'tronix) and 11x11x0.38 mm^3 SiO_2 coupons (Neyco) were placed on a stainless steel holder in the isothermal zone of the quartz tube. The evaporation steel chamber of the DLI system were heated to 200 °C to prevent precursors condensation. The DLI system (Kemstream) consists of a set of two injectors, one connected to a N_2-pressurized Schlenk flask for liquid injection in the mixing chamber, and one connected to a N_2-pressurized line for gas mixing of the solution droplet with N_2 and transfer to the evaporation chamber. The precursor solution was prepared in a Schlenk flask inside a glovebox circulated with purified Ar (99.9997%, Air Products) by adding a known amount of precursor into the flask. The sealed flask was taken out of the glovebox and completed with the appropriate quantity of anhydrous toluene (99.8%, H_2O<10ppm, Sigma-Aldrich) using an air-tight, Ar-purged, glass syringe to prepare the precursor solution. Then, the Schlenk flask was connected to the gas line and to the liquid injector inlet, and was purged several times with pressurized N_2 (99.9999%, Messer). The frequency and opening time of the injection system were set at 2 Hz and 3 ms, respectively, to feed the evaporation chamber with small precursor solution droplets mixed with N_2 gas with a mixing N_2 flow set at 400 standard cubic centimeter per minute (sccm). 600 sccm of O_2 (99.9999%, Messer) were added in the input gas prior

entering the deposition zone. Table 1 resumes the concentrations of the DLI solutions and the solutions flow to the deposition chamber for the three tested precursors.

Table 1. Concentrations of the DLI solutions and solutions flow to the deposition chamber for the three tested precursors.

	Precursor concentration in toluene (mol/L)	Precursor solution flow (mL/min)
TTIP	$4.0*10^{-2}$	0.5
1, $[TiO(thd)_2]_2$	$4.8*10^{-2}$	1.0
2, $Ti(OBu)_2(thd)_2$	$3.4*10^{-2}$	1.0

The film crystalline structure was measured by grazing incidence XRD (GIXRD) on a Bruker D8 Advance instrument, using a Cu K-α (λ = 1.5418 Å) X-ray tube operated at 40kV and 40 mA, a Ni filter, and solid-state Lynxeye detector in in θ+3° / θ-3° configuration. Samples were measured on a zero background holder and a θ offset of 3° was applied between the X-ray source and detector arms to suppress the strong (004) diffraction of the Si substrates normally measured around 69°. Photoelectron emission spectra were recorded using a monochromatised Al Kα (*hv* = 1486.6 eV) source on an ESCALAB 250 X-ray photoelectron spectroscopy (XPS) system with a 400 μm X-ray spot size. The spectra were calibrated in bond energy to the C–C/C–H bonds component of the carbon C1s peak at 284.6 eV (±0.1 eV). Depth profiles are realized by means of Ar^+ ions accelerated at 500 eV. The photoelectron peaks were analyzed by Gaussian/Lorentzian (G/L = 70/30) peak fitting and using a Shirley background. The atomic concentrations were determined from photoelectron peak areas using the atomic sensitivity factors reported by Scofield, taking into account the transmission function of the analyzer. This

function was calculated at different pass energies from Ag3d and AgMNN peaks collected for a silver reference sample. C concentrations, reported from these quantifications, are estimated to be exact within ±20%. Top view and cross sectional scanning electron microscopy (SEM) micrographs of the Pt-metalized samples were obtained with a field emission FESEM Jeol JSM 6700F instrument. Top view SEM images were investigated using spatial correlation and frequency analysis to quantify the morphological changes of TiO_2 surface micro and nanostructures. The analysis is performed with the nanoTOPO_SEM™ software provided by Nanometrisis. Spectroscopic ellipsometric (SE) measurements were performed using a Semilab SE-2000 apparatus. Resulting spectra are fitted using the appropriate effective medium approach anatase/rutile/void or anatase/void, in a two-layer construction, assuming carbon-free films. The transmission spectra of TiO_2 films deposited on fused silica substrates are investigated with a Agilent Cary 5000 double beam spectrophotometer in the Ultraviolet – visible range. The indirect and direct band-gap was deduced from the absorption spectra using the Tauc model for the TiO_2 anatase films and for the two-phase films, respectively. To evaluate the photocatalytic activity, TiO_2 samples deposited on Si from the three precursors are immersed in a water (65 %) – ethanol (35 %) v/v solution and irradiated during 60 h with a 300 Watt Xenon lamp. Production of hydrogen upon photocatalytic decomposition was analyzed with a gas chromatograph. Figure S1 in SI presents schematic and a photograph of the photocatalytic setup used for dihydrogen production.

3. Results and discussion

3.1. Evaluation of the volatility and thermal stability of the precursors

Figure 2 presents the thermogravimetric analysis of compounds **1** and **2**. The TGA results show mass loss with onset temperatures for **1** and **2** equal to 150 °C and 90 °C, respectively. Vaporization of **1** proceeds smoothly with a sharp mass loss after melting at ca. 320 °C, revealing low volatility but high thermal stability in the investigated conditions. Evaporation of **2** occurs at lower temperatures than **1** but mostly after melting. The mass loss curve of **2** reveals a two-step process with inflection at 250 °C, corresponding to the decomposition or oligomerization of the initial compound. The 50 % mass loss temperature of **1** occurs 115 degrees higher than that of 2 as shown in Table 2, which resumes the thermal and thermodynamic parameters of the vaporization of the three compounds. We attribute the low volatility of **1** to its dimeric nature [18], in contrast to the monomeric compound **2**. Both compounds show a small amount of nonvolatile residue, less than 10 % at 420 °C, thus revealing their convenient thermal stability.

The sublimation of **1** and **2** was investigated by Knudsen method at lower temperatures, namely 170-215 °C for **1** and 44-81 °C for **2**. The flow method was only applied to **1** in the temperature range 210-270 °C. Figure 2 presents the temperature dependence of the saturated vapor pressure in Arrhenius coordinates. The corresponding law for TTIP from Filatov et al. [24] is also reported for comparison. The observed results, namely the relative position of the experimental data are compatible with the trends revealed by TGA. The volatility of **1** and **2** is lower than that TTIP, justifying the use of DLI technology for the generation and transportation of vapors of the former two compounds.

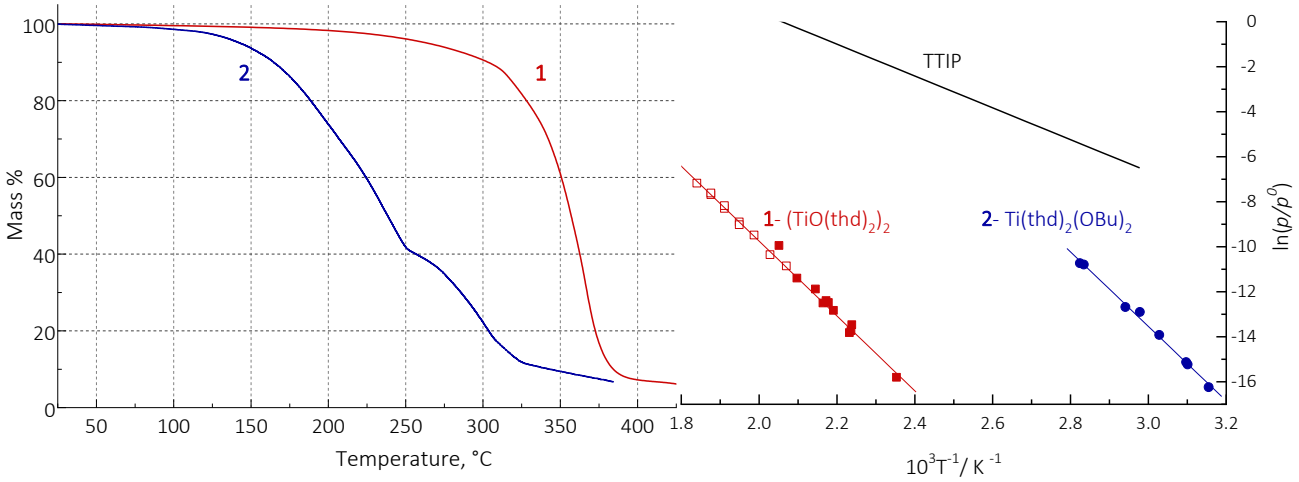

Figure 2. Sublimation behavior of compounds **1** and **2**. Mass loss vs. temperature, obtained from TGA (left), temperature dependent saturated vapor pressure (right). In the latter diagram, empty and full points correspond to the flow transportation and Knudsen methods, respectively.

The enthalpy and entropy of sublimation or evaporation obtained at the middle temperature of each temperature range of interest are reported in Table 2. We attribute the close sublimation enthalpies for **1** and **2** to the presence of identical ligands with bulky substituents in both compounds, resulting in similar intermolecular interactions. However, the values of sublimation entropy differ significantly, due to the sublimation of **1** as a dimer in contrast to **2**, which is sublimed as a monomer. The thermodynamic parameters for TTIP confirm its smooth evaporation in the liquid state.

Table 2. Thermal and thermodynamic properties of compounds **1**, **2** and TTIP.

Compound	Process	Method	N points T range, °C	$\ln (p/p^0) = A - B/T$		ΔH<T> kJ/mol	ΔS°<T> J/mol/K	TGA	
				A	B			T 50 % °C	Non-volatile residue @450°C wt %

1	Sublimation	Flow + Knudsen	21 174-270	23.57	16633	138±3	196±6	352	5
2	Sublimation	Knudsen	8 44 –81	36.05	16534	137±4	300±10	237	7
TTIP[24]	Evaporation		345-470	14.55	7068	58±3	121±5		

Table 3 resumes the main ion peaks obtained from mass spectrometric investigation of compound **1** with direct probe insertion and *in situ* analysis, at evaporator and reactor temperatures of 230 °C and 245 °C, respectively. The fingerprint of the thermal decomposition obtained from the *in situ* analysis differs from the rather simple signature, obtained through direct probing of the compound. It reveals a complex composition of the gas phase, attributed to the further, partial decomposition of the compound during its evaporation and transportation, despite its apparent stability concluded from the TGA analysis, at least in comparison with **2**. Such high number of intermediate species may affect the efficiency and control of the precursor transfer process to the deposition zone. Moreover, although all species contain directly bonded titanium and oxygen, the role and efficiency of each one in the surface reactions leading to the formation of the TiO_2 film is unclear.

Table 3. Main Ti-containing ion peaks and their relative intensities in mass spectra of compound **1**, obtained in vacuum.

Ion peak assignment	m/z	Intensity, %	
		Direct probe insertion	*In situ* analysis
$[Ti_2O_2(thd)_3]^+$	677	21	
$[(Ti(thd)_3]^+$	597	-	23
$[(Ti_2(thd)_2]$	462	12	23
$[O(TiO(thd))_2 - {}^tBu]^+$	453	-	27
$[TiO(thd)_2]^+$	430	13	50
$[O(Ti(thd))_2 - C_4H_8]^+$	422	-	100
$[(OTiO(thd))_2 - 2{}^tBu]^+$	396	-	41

$[TiO(thd)_2 - {}^tBu]^+$	373	100	68
$[O(Ti(thd))_2 - {}^tBu - C_4H_8)]^+$	365	-	45
$[OTi(thd)_2 - {}^tBu - C_3H_8)]^+$	329	6	-
$[TiO(thd)_2 - 2{}^tBu]^+$	316	-	82
$[O(TiO(thd))_2 - tBu - Hthd]^+$	269	-	27
$[Ti(OH)_2(thd)]^+$	265	4	-
$[TiO(thd)]^+$	247	43	40

We now investigate the composition of the gas phase of **1** in the presence of oxygen for different temperatures of the CVD reactor, at 235 °C fixed evaporator temperature. Figure 3 presents the evolution of the intensity as a function of the CVD reactor temperature of the main ion peaks identified in the mass spectra of the probed gas phase. Comparison of these results with those obtained in vacuum shows similar composition of the gas phase in the presence of oxygen, the main differences being the absence of $Ti(thd)_3$ and a larger amount of H_2O, CO and CO_2 at reactor temperatures higher than 300 °C. The intensity of Ti-containing peaks decreases and vanishes at 340 °C, revealing complete decomposition of **1** above this temperature. The main gaseous products of the decomposition are the protonated ligand H(thd) and, above 300 °C, butene C_4H_8, CO and CO_2. Oxygen peak intensity starts to decrease above 320 °C with further simultaneous increase of carbon oxides and water peaks, corresponding to the oxidation of the formed organic products.

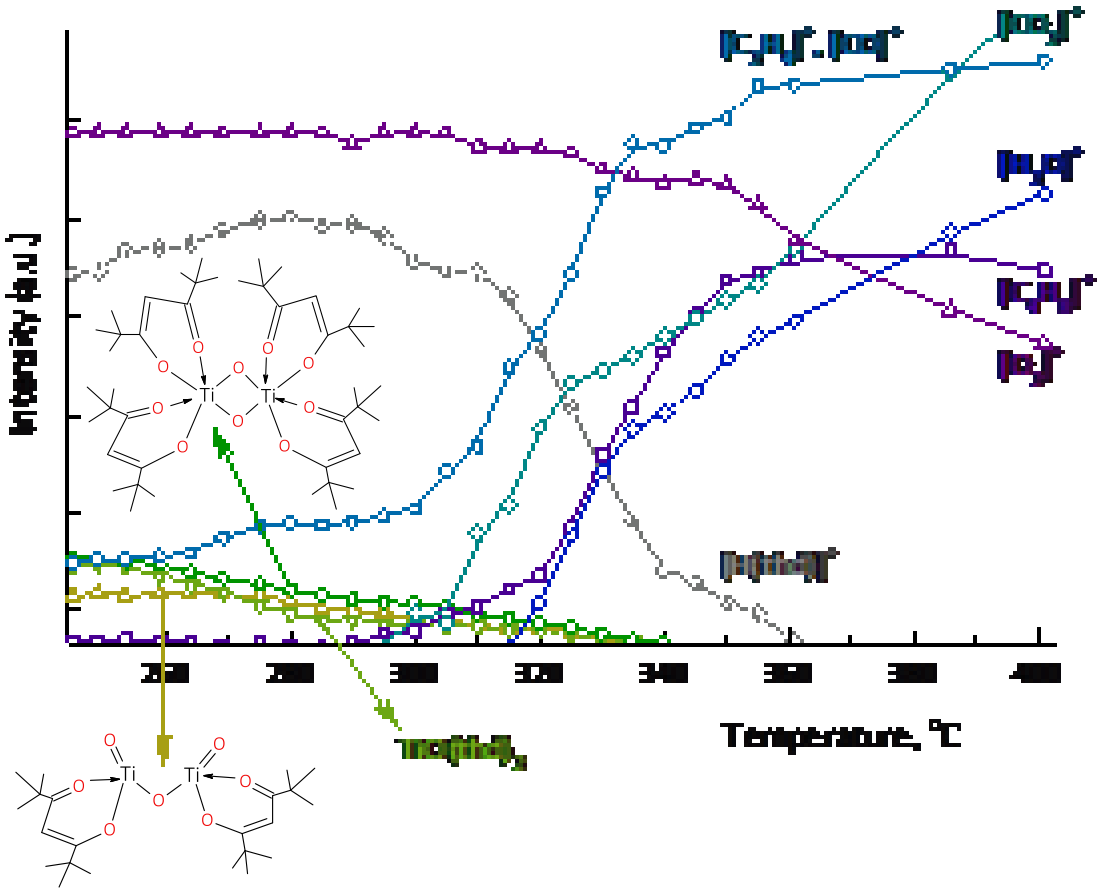

Figure 3. Evolution of the composition of the gas phase during the heterogeneous decomposition of **1**, in the presence of oxygen.

Due to its high volatility, **2** was analyzed by *in-situ* time-of-flight mass spectrometry, exclusively. We observed no changes in the mass spectra after three heating-cooling cycles between the ambient and 110 °C under dynamic vacuum conditions, demonstrating the long-term vaporization stability for the compound. Based on this behavior, the evaporator temperature was fixed at 110 °C and the evolution of the vaporized compound was monitored by varying the reactor temperature. Figure 4 presents mass spectra of **2** in the presence of oxygen, recorded at two reactor temperatures, 150 °C and 380 °C, corresponding to the absence and to the complete

thermolysis of the compound, respectively. At 150 °C the mass spectrum can be used as a reference spectrum for **2**. The assignment of the main Ti-containing peaks in this spectrum reveals that, in contrast to **1**, all ions are fragmentation products of the molecular ion $[Ti(OBu)_2(thd)_2]^+$; i.e. evaporation of compound **2** is congruent. In the mass spectrum at 380 °C there is no Ti- containing ion peaks corresponding to the entire precursor but water and carbon are observed together with a small amount of ^tBu. Figure 4 also shows the evolution of the intensities of the main ion peaks as a function of the reactor temperature. Decomposition of vaporized **2** begins at 190 °C, revealed by a sharp decrease of the intensity of the precursor peak and an increase in peak intensity of the observed products. We conclude that this temperature corresponds to the upper limit of the thermal stability of the precursor in the adopted operating conditions. In this diagram, the entire precursor is presented by the most intensive fragmentary ion peak $[Ti(thd)_2]^+$. Protonated β-diketonate H(thd), represented by the most intensive fragmentary ion, and ^tBu radical are the main fragmentation species in the initial mass spectrum. Their intensity increases with increasing temperature and then it decreases following the same trend as the Ti-containing fragments, indicating that, at this stage they are part of the thermal decomposition products. The intensity of the peaks of the initial compound is the lowest at 350 ° C, revealing the highest degree of decomposition at this temperature. Above 320 °C organic fragments are oxidized as shown by the strong decrease of their intensity and the simultaneous increase of the intensity of the peaks of water and carbon oxides and the decrease of that of oxygen. It is worth noting that, in the absence of oxygen we observe the same decomposition onset and gaseous products, with the exception of CO_2 and large amounts of H_2O and CO. We conclude that decomposition of vaporized compound **2** in the presence of oxygen occurs through

an intramolecular mechanism; oxygen interacts with organic products as is the case for compound **1**.

The comparison of the thermal behavior of compounds **1** and **2** reveals that long term heating of **1** is deleterious for its structural integrity. This difficulty can be minimized by drastically decreasing the duration of the vaporization and transport to the deposition zone of the precursor molecules, ensured by the DLI technology, provided oxygen is also fed downstream to obtain carbon-free films.

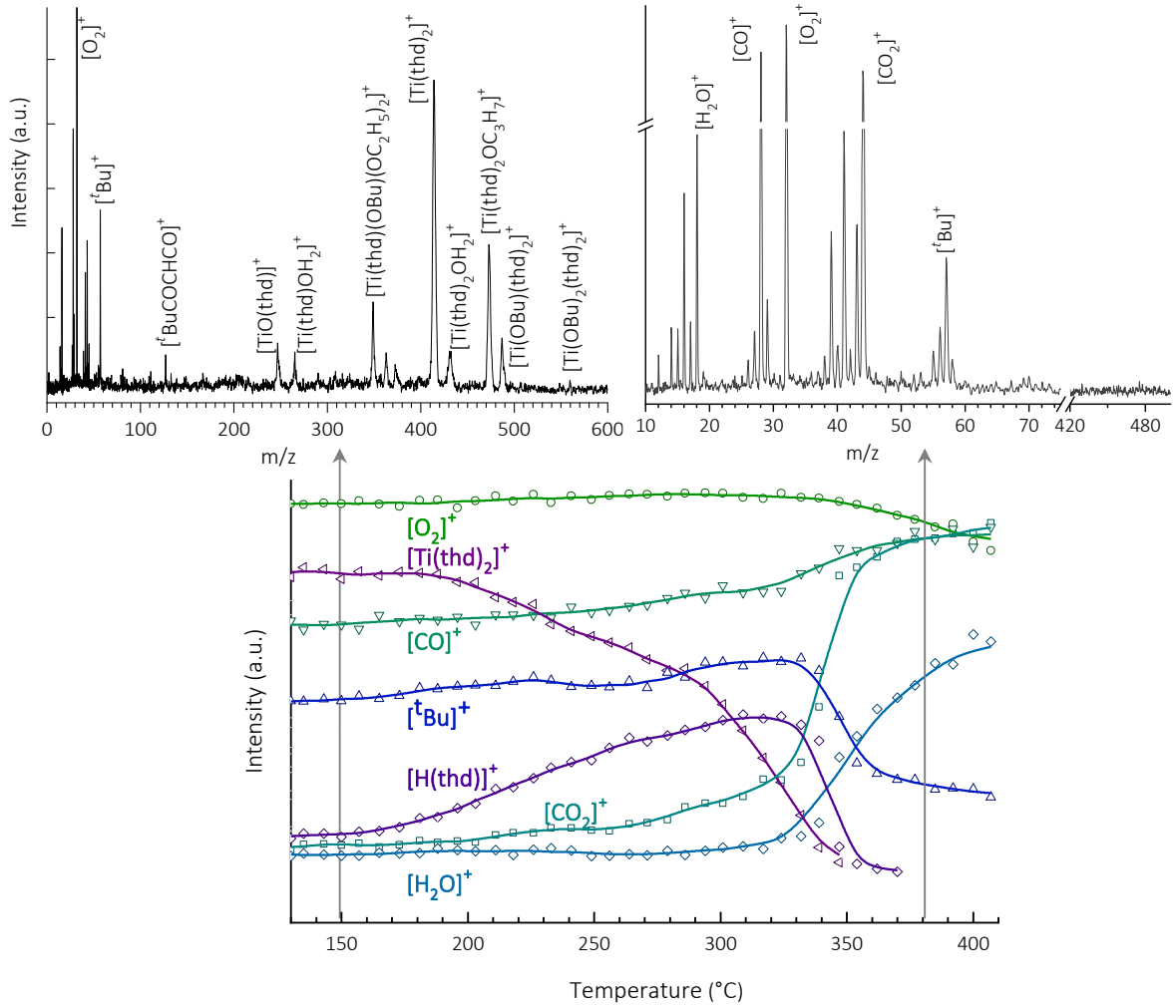

Figure 4. Mass spectra of the gas phase composed of vapors of **2** in the presence of oxygen, recorded at 150 °C and 380 °C. The two temperatures respectively correspond to the absence of decomposition and to complete decomposition of the compound. The diagram presents the evolution, as a function of the reactor temperature, of the main components of the gas phase in the same conditions. The diagram was built from continuously recorded mass spectra. As an example, arrows at 150 and 380 °C point on the source mass spectra at these temperatures.

3.2. Films composition and morphology

Figure 5 presents X-ray diffractograms of films processed from TTIP, **1** and **2**. The former yields pure anatase films, in agreement with literature reports on deposition of TiO_2 at this temperature, where TTIP was transported to the deposition area through simple vaporization from the liquid state [3, 5, 25, 26]. In contrast, DLI-MOCVD at 500 °C still from TTIP but without oxygen as gas-reactant results is a mixture of anatase and rutile in the films [10]. The X-ray diffractograms show that, in the same conditions precursors **1** and **2** result in films composed of a mixture of anatase and rutile revealing that, *ceteris paribus*, the composition of the films depends on the involved source chemistry, even in the presence of an external oxidant. Figure 5 also presents the result of the ellipsometric two layer model applied on representative films processed from the three precursors. The quality of the fit is 0.98 for films deposited from TTIP, and 0.97 for the two others. The upper, surface layer is systematically characterized by a significant percentage of voids and can be seen as a roughness layer. The thickness of this layer for the film deposited from TTIP is 51 nm, corresponding to 15 % of the total thickness. For the films processed from **1** and **2**, it is 31 nm and 39 nm, corresponding to 10 % and to 11 %, respectively, of the total thickness.

The porosity, corresponding to the voids, of the surface layer is 63 % for the film processed from TTIP, to be compared with 50-51 % for the films processed from **1** and **2**. Following the same trend, the porosity of the thicker, main layer by the substrate, is 36 % for the film processed from TTIP, to be compared with 16 % for the films processed from the two other precursors. Interestingly, the ellipsometric simulation results in the consideration of pure anatase for the film processed from TTIP, in contrast to the films processed from **1** and **2**, for which it results in a mixture of rutile and anatase, in agreement with the XRD results. The latter films are rich in rutile, the ratio of the latter phase over the sum of the two being 64 % and 63 %, respectively. We conclude that films deposited from precursors **1** and **2** are similar regarding the anatase to rutile ratio, and the amount and distribution of porosity. Their external layer is less extended and their entire structure is less porous than that of the pure anatase films deposited from TTIP.

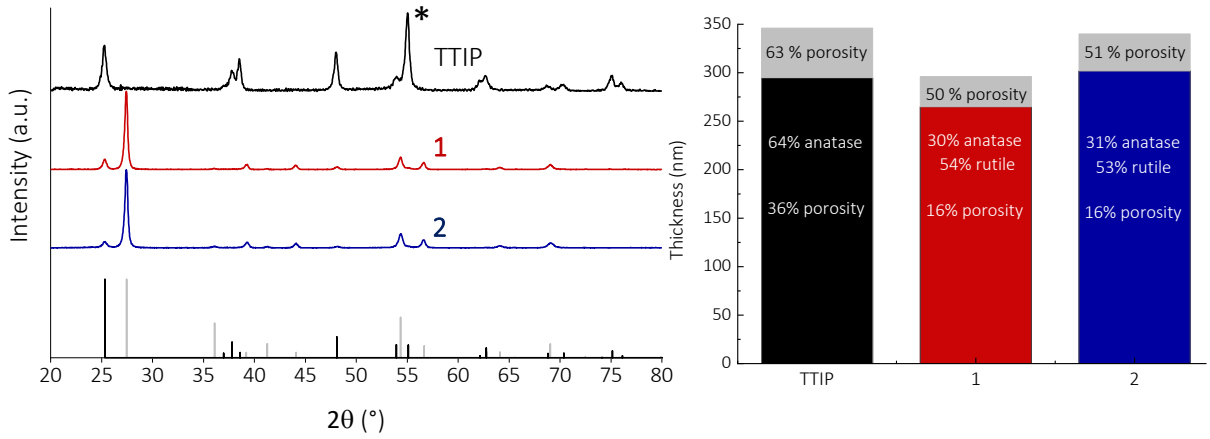

Figure 5. Left: Grazing incidence X-ray diffractograms of TiO_2 films deposited on Si from TTIP, **1** and **2**. The peak in asterisk corresponds to the Si substrate. The black and grey diffractograms in the lower part are the JCPDS files #99-100-9704 and #99-100-8659 of anatase and rutile, respectively. Right: Films thickness, structure, porosity and phase composition as simulated by spectroscopic ellipsometry from a two-layer model.

Figure 6 presents top surface and cross section SEM micrographs of films processed from the three precursors. Their thickness is similar, ranging from 280±30 to 320±30 nm corresponding to a deposition rate of 370, 320 and 370 nm/h from TTIP, **1** and **2**, respectively. The surface micrograph of the film processed from TTIP shows compact triangular superstructures, which match in the cross-section image the summits of the observed vertically oriented dendrites. Porosity is therefore observable between those dendrites, but also within each one, in small details shaping them into tree like items. This microstructure is comparable to the one obtained in the same conditions from vaporized TTIP [3]. Films from **1** and **2** are composed of vertical, sub-micronic aggregates having a flake shape, which are more densely packed. The observed morphologies prevail on the entire surface of the samples and are compatible with the ellipsometric simulations of the films. Indeed, the columnar morphology of the TTIP film confirms the high ratio of voids and subsequently reveals its high specific surface compared with the films processed from **1** and **2**, which present comparable morphologies.

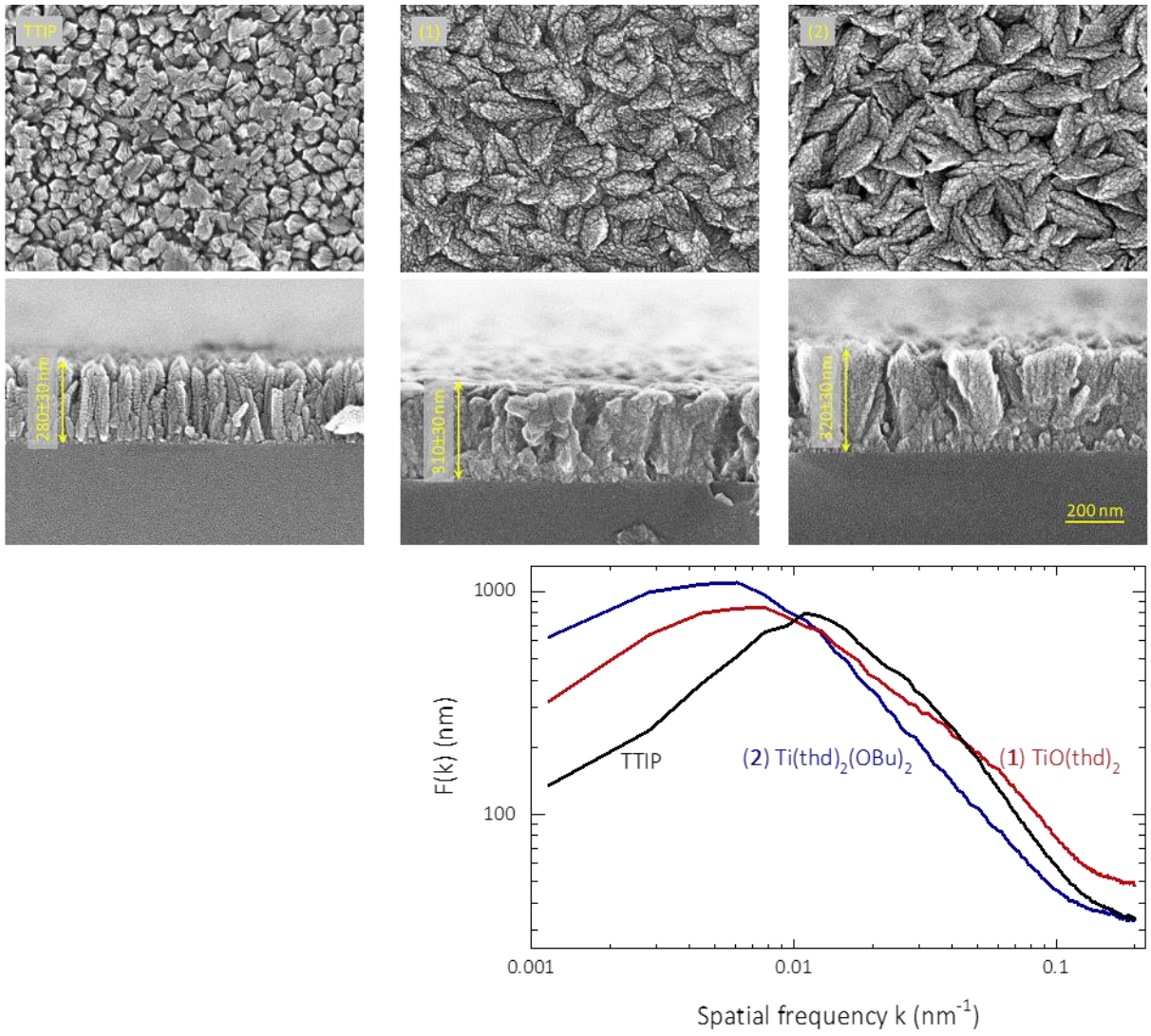

Figure 6. Top surface (upper line) and corresponding cross-section (middle line) field emission SEM micrographs of films deposited from TTIP (left), **1** (middle) and **2** (right). The magnification is the same for all micrographs and corresponds to the scale bar on the right. Fourier amplitude F(k) versus the total frequency $k = \sqrt{k_x^2 + k_y^2}$ for the top surface SEM micrographs of the three precursors (bottom).

A more detailed evaluation of the aggregate density and morphology can be achieved by means of the spatial Fourier analysis, performed top surface SEM micrographs like the ones of

figure 6, at five distinct points of each sample. The output of Fourier analysis is the Fourier spectra which quantify the contribution of spatial frequencies in film morphologies. Given the columnar structure of aggregates, the analysis of top SEM micrographs may also provide information about the whole 3D structure of deposited films since the structural variability along vertical direction is limited. The Fourier spectrum of a micrograph is actually a 2D function of the spatial frequencies k_x and k_y along the axes x and y respectively. However, due to the overall isotropy of the imaged structures, we can focus on the radial average of the 2D Fourier spectrum presenting the spatial frequency content of structures in a more straightforward manner. The bottom diagram of figure 6 displays the Fourier amplitude F(k) versus the total frequency $k = \sqrt{k_x^2 + k_y^2}$ for the SEM micrographs of the three precursors. In all cases, well-defined peaks are noticed revealing the approximate periodicity in the spatial arrangement of aggregates. The period of morphologies, i.e. the average spacing of aggregates, can be extracted by the inverse of peak frequency of Fourier spectra and is found to be smaller in TTIP structures (~92 nm) than in **1** and **2** (~130 nm and 163 nm respectively). This result is in conformity with the porosity measurements of ellipsometry since the smaller period of TTIP films found by Fourier analysis can be associated with more voids in the space between aggregates and hence higher porosity than **1** and **2**.

In addition, Fourier analysis proceeds further to detect differences in the apparently similar morphologies of **1** and **2** films: as it is previously noticed, period(**1**) is lower than period(**2**), which means that the films from **1** have smaller and more densely packed aggregates than those from **2**. This result will be recalled in the next subsections to contribute to the explanation of the higher H_2 photogeneration obtained by **1** films than from **2** films.

XPS measurements reveal the presence of C, in addition to Ti and O in all three films. Its mean composition in the subsurface zone of the films is 8.1, 10.0 and 6.4 at% for those deposited from TTIP, **1** and **2**, respectively. Figure 7 illustrates chemical bonds and compositional information obtained from XPS. The results are focused on the O1s and C1s high resolution spectra of all three samples acquired for six sputtering times between 0 s and 200 s, exemplified in the figure by the spectrum at 42 s of the film deposited from **1**. Deconvolution of the high resolution spectrum of the O1s peak reveals two components, one attributed to the O-Ti lattice at 530.5 eV and one to the non-lattice oxygen bonds at 531.9 eV, attributed to organic compounds with C–O or C=O [27, 28]. The O-Ti lattice part of the O1s peak, combined with the determined atomic fraction if Ti allows evaluating the O/Ti ratio in the TiO_2 structure of the three films. At the extreme surface of the film, this ratio is close to the stoichiometric value of 2, namely 2.10 for the one deposited from TTIP, 2.07 for those deposited from **1** and **2**. It continuously decreases with increasing sputtering time, with a steeper decrease for the film deposited from **2** than for the two others.

Deconvolution of the high resolution spectrum of the C1s peak reveals a predominant component at a binding energy of 285±0.1eV on all three samples, attributed to adventitious elemental carbon [29]. Two additional peaks appear at 289 eV and 286 eV. The former is attributed to carbon – oxygen carbonate bonds [30, 31], while the latter has been attributed to the Ti–C–O bond, based on previous literature reports [28]. It is worth noting that there is no peak observed at ca. 281 eV, thus excluding the presence of carbidic Ti–C bond in carbon-doped TiO_2. The evolution of the atomic concentration of the latter bond is presented in figure 7 as a function of sputtering time. At the extreme surface of the films, the concentration of the Ti–C–O bond is in the range 6-9 at%; it rapidly decreases to reach a steady value of ca. 2 at% for the three samples. Assuming that this peak indeed corresponds to the Ti–C–O bond, we cannot speculate any

physical reason for the variation of its concentration along the thickness of the three films. Further insight in the source references provided in [28], questions the unambiguous attribution of this peak to the Ti–C–O bond. We conclude that this binding energy refers both to the Ti–C–O bond and to aliphatic and/or adventitious carbon and that its observed evolution with sputtering time may indeed reveal a mixture of C-containing bonds. In that case, the remaining 2 at% concentration could be the effective "Ti–C–O" contribution.

Figure S2 in the SI section presents the evolution, as a function of sputtering time, of the part of the C1s peak attributed to the adventitious carbon, in the same conditions as the diagrams of figure 7. Expectedly, the surface concentration of this peak is predominant, at the level of 20 at% for the films deposited from TTIP, even 30 at% for the two others, due to the exposure of the samples to air before the XPS investigation. This surface pollution is also evidenced by the presence, within the O1s peak, of the component appearing at 531.9 eV. We observe a strong decrease of the concentration of adventitious carbon with increasing sputtering time without, however, reaching null concentration at any position along the film thickness. Instead, the adventitious carbon content seems to stabilize at ca. 5 at% for all three samples. The presence of aliphatic carbon in the core of such films has been previously reported [32]. It can be accounted for by the decomposition of the metalorganic precursors, the carbon of which is not fully removed during the growth, without excluding re-condensation on the fresh area of the sputtered carbon.

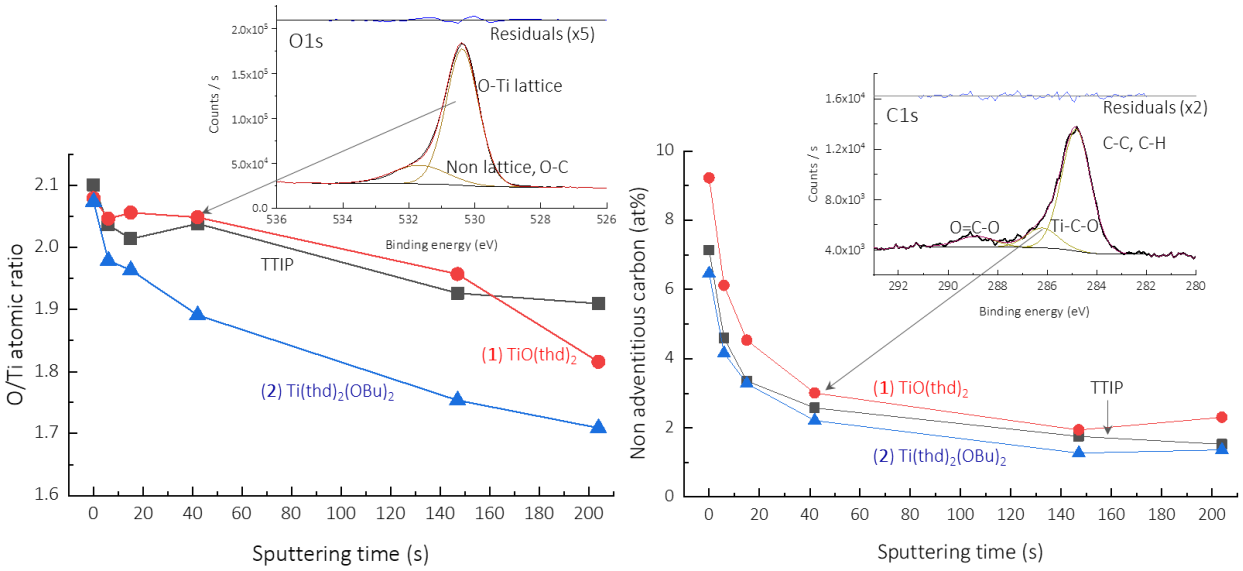

Figure 7. XPS analysis of the TiO2 films. Left: Evolution of the O/Ti atomic ratio as a function of sputtering time. The O concentration in the numerator is obtained from the O-Ti lattice part of the total O concentration, estimated from the deconvolution of the O1s high resolution spectra, exemplified in the figure by the spectrum at 42 s of the film deposited from 1. Right: Evolution of the atomic concentration of the Ti–C–O component of the carbon content of the film as a function of sputtering time. The Ti–C–O component of the carbon is obtained from the deconvolution of the C1s high resolution spectra, exemplified in the figure by the spectrum at 42 s of the film deposited from 1.

The optical bandgaps of the films processed from the three precursors were obtained from Tauc plots presented in Figure S3 in the SI section. We used indirect and direct Tauc representation for the TiO_2-anatase films and the two-phases films, respectively. The resulting values of 3.4 eV and 3.5 for films processed from rutile-rich **1** and **2**, respectively favorably compare with reported values of the direct band-gap energy of rutile (3.4 eV). Also, the value of 3.3 eV for the film processed from TTIP is in good agreement with the reported values of the

indirect band-gap energy of anatase (3.2 eV). The observed slight differences could be explained by the presence of interference fringes due to the low thickness of the films introducing a slight uncertainty in the band gap determination.

3.3. Photocatalytic tests

Figure 8 presents the amounts of photocatalyticaly produced H_2 as a function of time by the films deposited from TTIP, **1** and **2**. All films display constant H_2 production throughout the 60 h of the analysis, as shown by the linear trend of the curves, revealing high stability. After 60 h, the well-organized, nanotree-shaped anatase TiO_2 deposited from TTIP displays the highest cumulative H_2 production of 5.5 $mmol.m^{-2}$. After the same duration, the anatase-rutile film deposited from **1** shows a production of only 3 $mmol.m^{-2}$; i.e. almost half of the pure anatase film. Despite the similar composition and morphology, the film deposited from **2** demonstrates an even lower H_2 production of 1 $mmol.m^{-2}$.

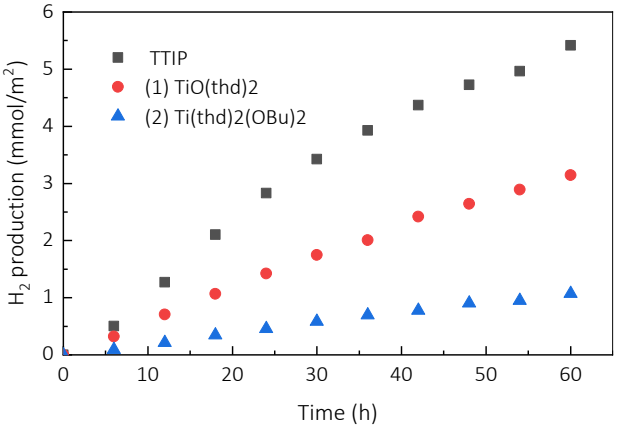

Figure 8. H_2 photogeneration as a function of time of the TiO_2 films obtained from TTIP, **1** ($TiO(thd)_2$, **2** ($Ti(thd)_2(OBu)_2$) precursors.

4. Discussion

The comparison of the vaporization and transport behaviors between **1** and **2** reveals a higher overall stability of the former in the vaporization process, counterbalanced, by a wealth of probed ion peaks at moderate temperature (230 °C) for **1** compared with the straightforward, congruent vaporization of **2**. These differences should affect the efficiency and control of the precursor transfer process to the deposition zone. However, they do not seem to influence the composition and the structural characteristics of the films, which remain comparable in the investigated deposition conditions, in terms of nature and composition of phases present and their morphological characteristics such as porosity and surface roughness. It is worth noting that the deposition rate from **1** is lower, despite the presence of two titanium atoms in the dimeric structure of **1** and one in **2**, and the higher precursor concentration of **1** in the solution flow to the deposition zone ($4.8*10^{-2}$ vs. $3.4*10^{-2}$ mol/L). This trend has been observed independently by ellipsometry and in SEM cross sections. The same trend was obtained from the mass gain of the samples, measured by weighting them before and after deposition, considering the volume percentage of rutile and anatase in the films (Figure 5) and the densities of the two phases. This difference can be attributed to the partial decomposition of **1** during its evaporation and transportation, resulting in numerous intermediate species, part of which may not participate in the deposition mechanism.

The deposition of rutile-rich TiO_2 films from **1** and **2** in the same conditions for which TTIP yields pure anatase films is worth noticing. The corresponding mechanisms that monitor the competitive growth of anatase and rutile phases from different precursors are still unclear and may involve the nature and the initial chemical state of the substrate. For example, Bessergenev et al. deposited pure anatase films on silicon dioxide substrates at 520 °C; i.e. just 20 degrees above the present process temperature, from $Ti(O^iPr)_2(thd)_2$ an heteroleptic precursor which is

structurally close to **2** [33]. The same group reported later the formation of rutile at 450-500 °C on different substrates under varied conditions [25].

TiO_2 films deposited from **2** present significant lower photocatalytic activity than those deposited from **1**, despite the fact that they are both composed of similar rutile to anatase ratios. This difference can be attributed to morphological differences between the two films since, according to the results of Fourier analysis, the film from **1** is characterized by smaller periods than **2**. Such a smaller period leads to denser aggregate and pore networks and therefore higher specific area and consequently more H_2 photogeneration rate. It can also attributed to the noticeable difference in the O/Ti ratio in their TiO_2 structure, which is lower by 0.2 for **2**. Due to artefacts induced by the Ar^+ sputtering, it is not possible to correlate such lower O/Ti ratio in **2** to a lower oxidation degree of the Ti cation.

Both films deposited from **1** and **2** present a lower photocatalytic activity than the one deposited from TTIP. The most straightforward reason for this is their significant rutile content, to be compared with the pure anatase composition of the film from TTIP. However, the complexity of such engineering materials underlines additional reasons for this difference. For example, the morphological differences can account for this, namely the higher open porosity of the film deposited from TTIP, which allows extended contact with the liquid per unit surface, in contrast to the smaller and more densely packed aggregates for the films from **1** and **2**. Finally yet importantly, the film deposited from TTIP present significantly lower amount of adventitious carbon on its extreme surface than those from **1** and **2** (figure S2).

The present work confirms that MOCVD of TiO_2 is at least temperature- and precursor- specific [13] and reveals the importance of the involved chemistry in the structural and functional characteristics of the films. More precisely, it provides a chemistry tool to monitor the rutile to anatase ratio in the films together with their microstructure in a moderate process temperature,

which yields pure anatase films from the classical TTIP precursor. We show that such differences have a noticeable influence of the generation rate of H_2 in the photocatalytic decomposition of water.

In a general perspective, this work contributes to the structuring of the materials data base for the TiO_2 films. As it has been reported by Butenko and Meredig in a recent materials by design roadmap [16], materials data are actually distributed across many small, isolated data silos. This raises the question of systematic way of determining quantitative metrics characterizing the level of similarity among similar materials and among their fabrication processes. Although at lesser extend than a combinatorial approach, the present work can serve as a paradigm of structuring experimental data that can be useful to build new models for extended and more reliable predictions in the process-structure-properties relationship. Hence, such advances in experimental methodologies combined with analogous computational ones can revolutionize our understanding of modern materials and their deployment in breakthrough applications.

5. Conclusions

We investigated two MOCVD solid precursors, namely oxo-β-diketonate $TiO(thd)_2$ (**1**) and alkoxide-β-diketonate $Ti(thd)_2(OBu)_2$ (**2**), and we compare them to TTIP, the seminal precursor for the deposition of TiO_2 films. **1** and **2** present different thermal stability and thermolysis mechanisms in the gas phase, with 150 °C onset vaporization temperature of **1** in the form of dimer: i.e. 60 degrees higher than that of **2**, which is sublimed as a monomer. Despite this apparent less pronounced thermal stability, vaporization of **2** occurs congruently, in contrast to the vaporization of **1**, which results in a complex mixture of intermediate species that may affect the efficiency and control of the precursor transfer process to the deposition zone. In order to face such thermal sensitivity and subsequent instability, we used direct liquid injection to feed the

deposition zone of the CVD setup with precursor vapors. Deposition from **1** and **2** in identical conditions, namely 500 °C and 1.33 kPa, resulted in rutile rich, rutile-anatase TiO_2 films. Deposition in the same conditions from TTIP expectedly resulted in pure anatase films. The morphological characteristics of the films also present significant differences, namely large grains with less voids in the space between building blocks and consequently lower porosity for those deposited from **1** and **2** (16 %) compared to the inter- and intra-columnar porosity of the film deposited from TTIP (36 %). Despite the overall similarities, films deposited from **1** present smaller and more densely packed aggregates than those from **2**. All films contain 5 at% aliphatic carbon that can be accounted for by the decomposition of the metalorganic precursors, the carbon of which is not fully removed during the growth. Additional 2 at % of carbon is inserted in the Ti-O network to form Ti-C-O bonds. The O/Ti ratio in the O-Ti lattice is 0.2 units lower for those deposited from **2**. This difference, together with morphological differences between the two films revealed by Fourier analysis of surface SEM micrographs may explain a lower generation rate of H_2 of films from **2**, in the photocatalytic decomposition of water. In a larger perspective, such coherently organized experimental information can be useful to build new models for extended and more reliable predictions in the process-structure-properties relationship.

Author Contributions

D.S. and V.K. preformed the CVD experiments and structural characterization of the films. A.T. performed MS measurements and analysis. A.M. performed structural characterization of the films. J.C. performed SWS experiments. S.S. performed vapor pressure measurements and thermodynamic calculations, S.T. performed Knudsen cell measurements, P.S. synthesized the molecular compounds. J.E. performed and analyzed XPS measurements. V.C. performed image analysis of surface micrographs. C.V. supervised the work. The manuscript was written through

contributions of all authors. All authors have given approval to the final version of the manuscript.

Acknowledgement

This work was supported by RFBR and CNRS through grants #18-53-15005, and PRC 1986/2018, respectively.

References

1. U. Diebold, *Surf. Sci. Rep.*, 2003, **48**, 53-229.

2. A. Fujishima and K. Honda, *Nature*, 1972, **238**, 37-38.

3. A. Miquelot, O. Debieu, V. Rouessac, C. Villeneuve, N. Prud'homme, J. Cure, V. Constantoudis, G. Papavieros, S. Roualdes and C. Vahlas, *Appl. Surf. Sci.*, 2019, **494**, 1127-1137.

4. A. M. Alotaibi, S. Sathasivam, B. A. D. Williamson, A. Kafizas, C. Sotelo-Vazquez, A. Taylor, D. O. Scanlon and I. P. Parkin, *Chem. Mater.*, 2018, **30**, 1353-1361.

5. Z. S. Khalifa, *Surf. Rev. Lett.*, 2016, **23**.

6. Y. Chimupala, P. Junploy, T. Hardcastle, A. Westwood, A. Scott, B. Johnson and R. Brydson, *J. Mat. Chem. A*, 2016, **4**, 5685-5699.

7. F. D. Duminica, F. Maury and F. Senocq, *Surf. Coat. Techn.*, 2004, **188**, 255-259.

8. M. Regue, S. Sibby, I. Y. Ahmet, D. Friedrich, F. F. Abdi, A. L. Johnson and S. Eslava, *J. Mat. Chem. A*, 2019, **7**, 19161-19172.

9. M. L. Hitchman and F. Tian, *J. Electroanal. Chem.*, 2002, **538**, 165-172.

10. S. P. Krumdieck, R. Boichot, R. Gorthy, J. G. Land, S. Lay, A. J. Gardecka, M. I. J. Polson, A. Wasa, J. E. Aitken, J. A. Heinemann, G. Renou, G. Berthome, F. Charlot, T. Encinas, M. Braccini and C. M. Bishop, *Sci. Rep.*, 2019, **9**.

11. S. Krumdieck, R. Gorthy, A. J. Gardecka, D. Lee, S. S. Miya, S. D. Talwar, M. I. J. Poison and C. Bishop, *Surf. Coat. Techn.*, 2017, **326**, 402-410.

12. F. D. Duminica, F. Maury and R. Hausbrand, *Surf. Coat. Technol.*, 2007, **201**, 9304-9308.

13. C. J. Taylor, D. C. Gilmer, D. G. Colombo, G. D. Wilk, S. A. Campbell, J. Roberts and W. L. Gladfelter, *J. Am. Chem. Soc.*, 1999, **121**, 5220-5229.

14. M. Taylor, R. C. Pullar, I. P. Parkin and C. Piccirillo, *J. Photochem. Photobiol., A*, 2020, **400**, 112727.

15. J. Altmayer, S. Barth and S. Mathur, *RSC Advances*, 2013, **3**, 11234-11239.

16. K. Alberi, M. B. Nardelli, A. Zakutayev, L. Mitas, S. Curtarolo, A. Jain, M. Fornari, N. Marzari, I. Takeuchi, M. L. Green, M. Kanatzidis, M. F. Toney, S. Butenko, B. Meredig, S. Lany, U. Kattner, A. Davydov, E. S. Toberer, V. Stevanovic, A. Walsh, N. G. Park, A. Aspuru-Guzik, D. P. Tabor, J. Nelson, J. Murphy, A. Setlur, J. Gregoire, H. Li, R. J. Xiao, A. Ludwig, L. W. Martin, A. M. Rappe, S. H. Wei and J. Perkins, *J. Phys. D: Appl. Phys.*, 2019, **52**.

17. B. J. Blackburn, C. Drosos, D. B. Brett, M. A. Parkes, C. J. Carmalt and I. P. Parkin, *RSC Advances*, 2016, **6**, 111797-111805.

18. N. B. Morozova, A. E. Turgambaeva, I. A. Baidina, V. V. Krysyuk and I. K. Igumenov, *J. Struct. Chem.*, 2005, **46**, 1047-1051.

19. V. V. Krisyuk, S. V. Sysoev, A. E. Turgambaeva, A. A. Nazarova, T. P. Koretskaya, I. K. Igumenov and N. B. Morozova, *J. Therm. Anal. Calorim.*, 2017, **130**, 1105-1110.

20. P. P. Semyannikov, I. K. Igumenov, S. V. Trubin, T. P. Chusova and Z. I. Semenova, *Thermochim. Acta*, 2005, **432**, 91-98.

21. A. E. Turgambaeva and I. K. Igumenov, *J. Phys. IV*, 2001, **11**, 621-628.

22. A. E. Turgambaeva, V. V. Krisyuk, N. Prud'homme and C. Vahlas, *ECS Trans.*, 2009, **25**, 1301-1308.

23. L. Baggetto, C. Charvillat, J. Esvan, Y. Thébault, D. Samélor, H. Vergnes, B. Caussat, A. Gleizes and C. Vahlas, *Chem. Vap. Dep.*, 2015, **21**, 343-351.

24. E. S. Filatov, H. Nizard, P. P. Semyannikov, S. V. Sysoev, S. V. Trubin, N. B. Morozova, K. V. Zherikova and N. V. Gelfond, in *Eurocvd 17 / Cvd 17*, eds. M. T. Swihart, D. Barreca, R. A. Adomaitis and K. Worhoff, 2009, vol. 25, pp. 557-560.

25. V. G. Bessergenev, R. J. F. Pereira, M. C. Mateus, L. Khmelinskii, D. A. Vasconcelos, R. Nicula, E. Burkel, A. M. B. do Rego and A. I. Saprykin, *Thin Solid Films*, 2006, **503**, 29-39.

26. S. Yamauchi, K. Ishibashi and S. Hatakeyama, *J. Cryst. Process Technol.*, 2014, **4**, 185-192.

27. K. S. Raja, T. Gandhi and M. Misra, *Electrochem. Commun.*, 2007, **9**, 1069-1076.

28. B. Yang, C. K. Ng, M. K. Fung, C. C. Ling, A. B. Djurišić and S. Fung, *Mat. Chem. Phys.*, 2011, **130**, 1227-1231.

29. X. X. Wang, S. Meng, X. L. Zhang, H. T. Wang, W. Zhong and Q. G. Du, *Chem. Phys. Lett.*, 2007, **444**, 292-296.

30. X. X. Yang, C. D. Cao, L. Erickson, K. Hohn, R. Maghirang and K. Klabunde, *J. Catal.*, 2008, **260**, 128-133.

31. S. Sakthivel and H. Kisch, *Angew. Chem. Int. Ed.*, 2003, **42**, 4908-4911.

32. P. Babelon, A. S. Dequiedt, H. Mostéfa-Sba, S. Bourgeois, P. Sibillot and M. Sacilotti, *Thin Solid Films*, 1998, **322**, 63-67.

33. V. G. Bessergenev, I. V. Khmelinskii, R. J. F. Pereira, V. V. Krisuk, A. E. Turgambaeva and I. K. Igumenov, *Vacuum*, 2002, **64**, 275-279.

Graphical Abstract

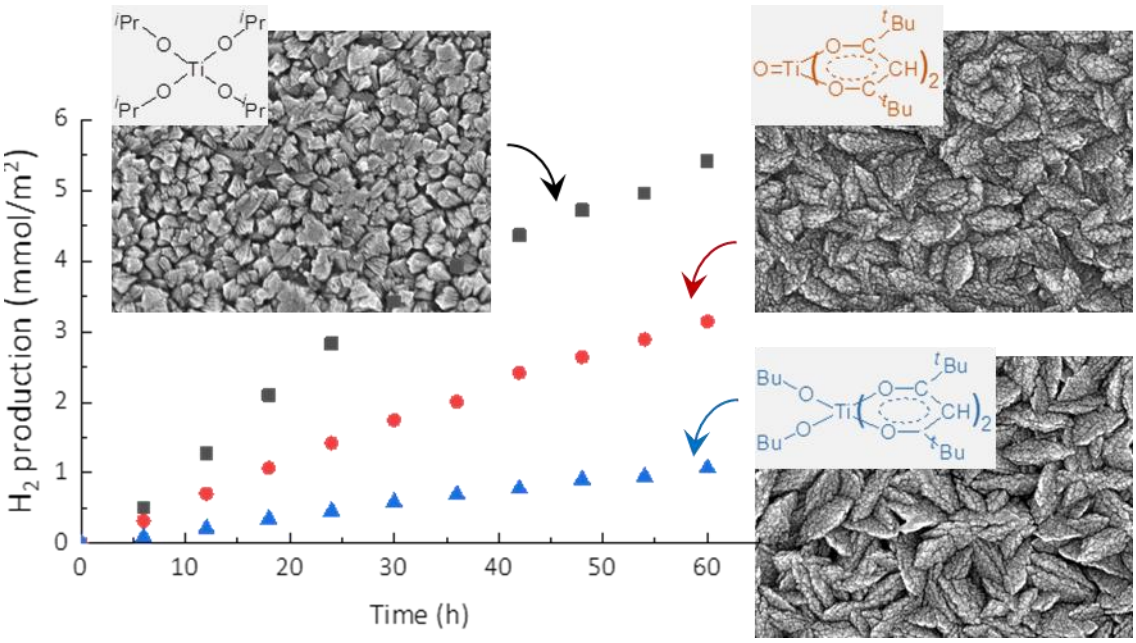

Electronic Supplementary Material (ESI) for CrystEngComm.

SUPPORTING INFORMATION FOR THE MANUSCRIPT

Engineering structure and functionalities of chemical vapor deposited photocatalytic titanium dioxide films through different types of precursors

Diane Samélor[1], Asiya Turgambaeva[2], Vladislav Krisyuk[2], Adeline Miquelot[1], Jeremy Cure[3], Sergey Sysoev[2], Sergey Trubin[2], Pavel Stabnikov[2], Jérôme Esvan[1], Vassilios Constandoudis[4], Constantin Vahlas[1,*]

[1] *CIRIMAT-CNRS, 4 allée Emile Monso, BP-44362, 31030 Toulouse Cedex 4, France*

[2] *Nikolaev Institute of Inorganic Chemistry SB RAS, Novosibirsk 630090, Russia*

[3] *LAAS-CNRS, Avenue du Colonel Roche, 31031 Toulouse, France*

[4] *Nanometrisis, TEPA Lefkippos, Patriarchou Grigoriou & Neapoleos 27, PO Box 60037, Agia Paraskevi 15341, Greece*

[*] *Corresponding author. constantin.vahlas@ensiacet.fr*

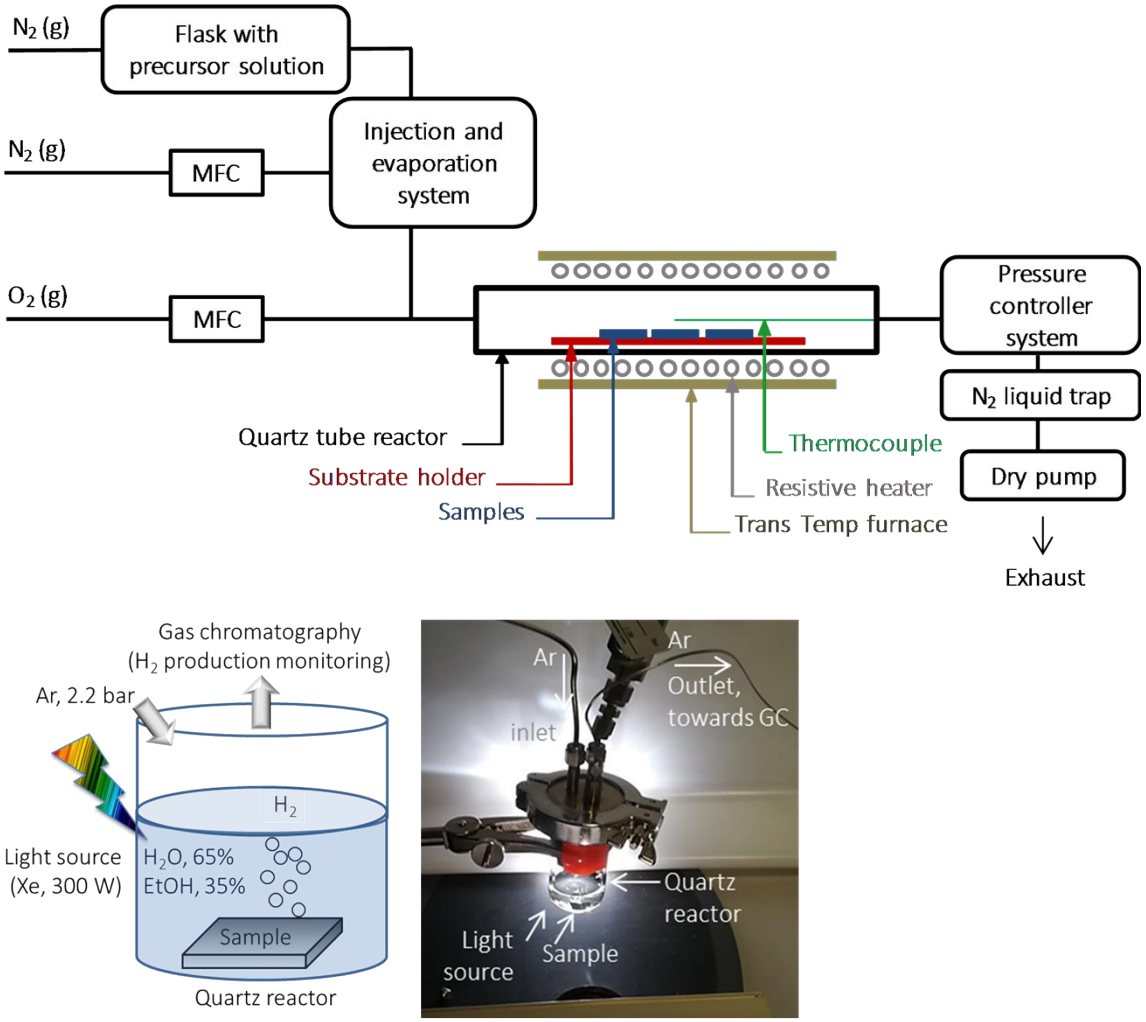

Figure S1. Schematic view of the CVD reactor (top) and schematic and a photograph of the photocatalytic setup used for dihydrogen production (bottom).

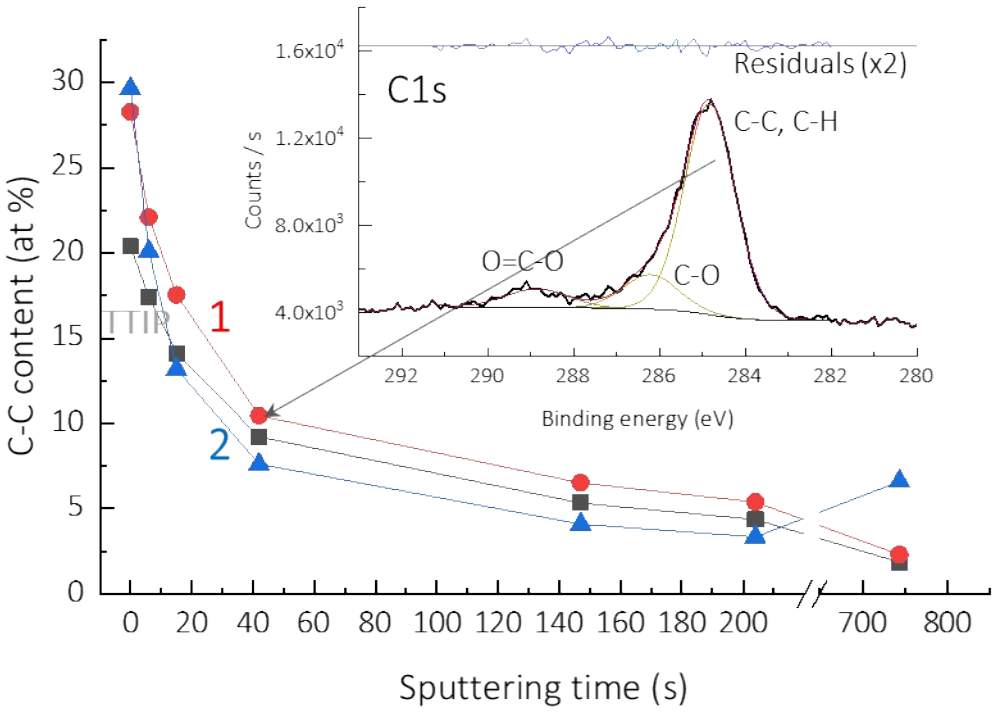

Figure S2. Evolution of the atomic concentration of the C-C component of the carbon content of the film as a function of sputtering time. The C-C/C-H component is obtained from the deconvolution of the C1s high resolution spectra, exemplified in the figure by the spectrum at 42 s of the film deposited from **1**.

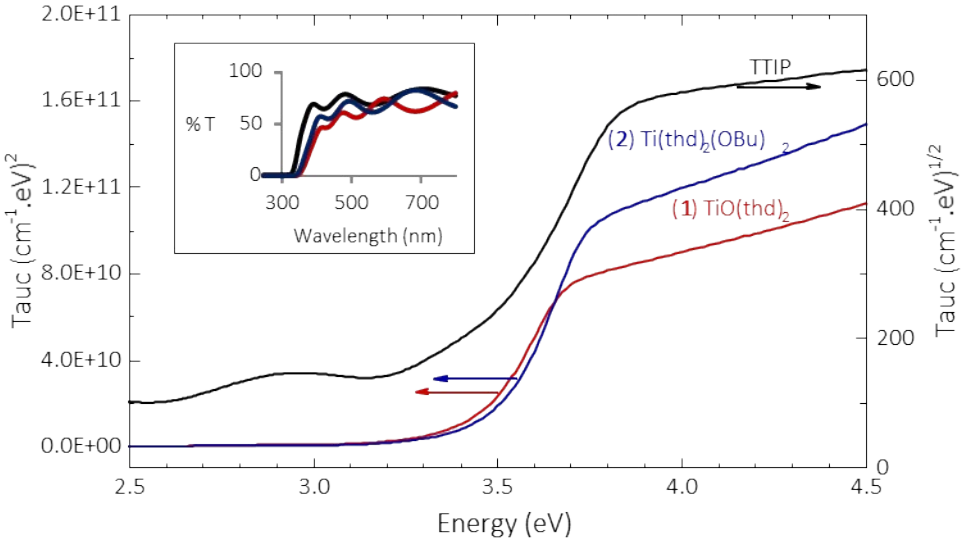

Figure S3. Tauc plots of the absorption coefficient determined by UV-Vis transmission spectroscopy for films deposited from the three precursors. Transmittance spectra of the films are in insert.